

# Modelling and simulation of electro-mechanically coupled dielectric elastomers and myocardial tissue using smoothed finite element methods

Tan Tran<sup>a</sup>, Denisa Martonová<sup>b</sup>, Sigrid Leyendecker<sup>a</sup>

<sup>a</sup>*Friedrich-Alexander-Universität Erlangen-Nürnberg, Institute of Applied Dynamics, Immwahrstraße 1, 91058 Erlangen, Germany*

<sup>b</sup>*Friedrich-Alexander-Universität Erlangen-Nürnberg, Institute of Applied Mechanics, Egerlandstraße 5, 91058 Erlangen, Germany*

---

## Abstract

Computational modelling offers a cost-effective and time-efficient alternative to experimental studies in biomedical engineering. In cardiac electro-mechanics, finite element method (FEM)-based simulations provide valuable insights into diseased tissue behaviour and the development of assistive systems such as dielectric elastomer actuators. However, the use of automatically generated tetrahedral meshes, commonly applied due to geometric complexity, often leads to numerical issues including overly stiff responses and volume locking, particularly in incompressible materials. Smoothed finite element methods (S-FEMs) offer a promising alternative by softening the stiffness matrix through gradient smoothing over defined smoothing domains. This work extends S-FEM formulations to electro-mechanically coupled problems and compares their performance against standard linear FEM. We implement and evaluate four approaches in the Abaqus environment via custom user elements: standard linear FEM, face-based S-FEM (FS-FEM), node-based S-FEM (NS-FEM), and the hybrid face/node-based S-FEM (FSNS-FEM). Two benchmark problems are studied: the electrically induced contraction of a compressible dielectric elastomer and an incompressible, orthotropic myocardial tissue sample. Reference solutions are obtained using a mesh consisting of higher-order elements. Our results demonstrate that FSNS-FEM provides the best balance between accuracy and computational efficiency, closely matching reference data. NS-FEM produces softer results, which leads to an overestimation of the true deformation. FS-FEM and standard FEM consistently exhibit overly stiff behaviour, with pronounced volume locking in the myocardial case. These findings support the potential of S-FEMs, in particular FSNS-FEM, for accurate simulation of coupled electro-mechanical behaviour in complex biomedical applications.

---

## 1. Introduction

Cardiovascular diseases represent the leading cause of death worldwide, accounting for approximately 17.9 million deaths in 2019, according to estimates by the World Health Organization [29]. They comprise a broad spectrum of pathological conditions involving the heart and vascular system, with ischaemic heart disease and stroke being the most prevalent manifestations [26]. At the core of cardiac function lies a coupled electro-mechanical process: an electrical signal propagates through the cardiac tissue, initiating the contraction of cardiac muscle cells, cardiomyocytes, which in turn drives the mechanical action of blood circulation. This coupling between electrical excitation and mechanical contraction, referred to as excitation-contraction coupling, is fundamental to the normal functioning of myocardial tissue. Capturing this phenomenon through computational modelling is essential for advancing our understanding of cardiac mechanics and electrophysiology, and for evaluating the behavior of biologically inspired materials under coupled field conditions. The finite element method (FEM) is widely employed in the simulation of biological tissues due to its ability to handle complex geometries, heterogeneous materials, and nonlinear deformation. Particularly in cardiac applications, tetrahedral (TET) meshes are favored due to their adaptability to intricate anatomical shapes, and can be efficiently generated via algorithms such as Delaunay triangulation. However, the use of linear TET elements in nearly incompressible soft tissue often leads to well-known numerical issues such as volumetric locking and overly stiff behavior [13]. Remedies for these challenges include the use of higher-order elements or significantly refined meshes, both of which increase computational cost. An alternative approach is the smoothed finite element method (S-FEM), which combines aspects of mesh-free methods with conventional FEM techniques [14, 13, 18, 19]. S-FEM improves solution accuracy and convergence properties without the need for mesh refinement or higher-order basis functions. In contrast to standard FEM, where strains and stresses are derived element-wise, S-FEM computes smoothed gradients over specifically defined smoothing domains (SDs), which are constructed based on the original mesh topology. Depending on the SD configuration, several S-FEM variants exist. For three-dimensional (3D) problems, commonly used schemes include face-based S-FEM (FS-FEM) introduced by [24], node-based S-FEM (NS-FEM) introduced by [16], and hybrid schemes such as the face-node selective S-FEM (FSNS-FEM) proposed by [11]. Previous studies have demonstrated the effectiveness of S-FEM for modeling large deformation of soft, anisotropic, and incompressible materials, including biological tissues. For instance, FS-FEM has been applied to hyperelastic tissue modeling [22] and mechanical simulations of soft organs [21]. FSNS-FEM and edge-node schemes have also been implemented in models of passive myocardium with complex fibre orientations [11, 12]. Further, different S-FEM techniques have been used in simulation of active cardiac mechanics modelled with a time-dependent, rather than potential-dependent, active stress [18, 19]. In summary, all of these applications treat the mechanical problem in isolation, without explicitly accounting for the coupling between

electrical and mechanical domains. Recently, S-FEM has been successfully extended to electro-mechanical coupling, but only so far in piezoelectric contexts using cell-based smoothing domains [3, 32]. While several finite element formulations exist for electro-mechanically coupled dielectric elastomers [8, 28] and cardiac tissue [7, 19], these methods predominantly rely on standard FEM discretisations. To date, no work has demonstrated the application of S-FEMs to such coupled problems involving dielectric elastomers or cardiac tissue and a systematic comparison across different S-FEM variants in this context remains unexplored. This highlights a research gap and provides the motivation for the current study. The goal of this work is to develop and evaluate S-FEM-based formulations for modeling electro-mechanically coupled problems in soft dielectric and biological materials. Specifically, we implement FS-FEM, NS-FEM, and FSNS-FEM using linear tetrahedral meshes, and compare their performance against standard TET-FEM. The study focuses on both numerical accuracy and computational efficiency in the context of large-deformation simulations. This paper is organised as follows: First, we introduce the continuum mechanics framework, including the strong and weak forms of the governing electro-mechanical equations. Second, we present the constitutive models for hyperelastic, incompressible dielectric elastomers and myocardial tissue. Third, we outline the numerical solution strategy, describe the integration of S-FEM into the iterative finite element solver, and summarise implementation details. Finally, two benchmark problems are simulated: an electro-active dielectric elastomer cube and a prolate ellipsoidal myocardial segment. Results are compared across the FEM and S-FEM schemes to assess differences in solution quality and computational cost.

## 2. Coupled problem formulation

In this section, we state the fundamental equations and continuum mechanical framework to describe the electro-mechanically coupled problem for the dielectric elastomer and the myocardial tissue. First, we introduce fundamental kinematic quantities to describe the large deformation of soft material. Then, the partial differential equations (PDEs) are stated for the electrical polarisation and mechanical deformation. To later apply the numerical methods, we also introduce the weak forms of the governing PDEs.

### 2.1. Kinematics of large deformations

To describe large deformations, we introduce fundamental quantities based on the finite strain theory which is part of non-linear continuum mechanics. For further information regarding the formulas and theorems, the reader is referred to [2, 30].

Let us first consider an undeformed body in the material configuration  $\mathcal{B}_0$ . Points inside  $\mathcal{B}_0$  are described by material coordinates  $\mathbf{X}(t_0) = \mathbf{X}$  for a given initial time  $t_0$ . The deformed body is set in the spatial configuration  $\mathcal{B}$  where the position of a point is described by the corresponding spatial coordinates

$\mathbf{x} = \mathbf{x}(\mathbf{X}, t)$  at a certain time  $t \geq t_0$ . The spatial coordinates can be considered as unique and continuous differential mappings of the material coordinates from  $\mathcal{B}_0$  to  $\mathcal{B}$  with

$$\mathbf{x} : \mathcal{B}_0 \rightarrow \mathcal{B}, \quad \mathbf{X} \mapsto \mathbf{x}(\mathbf{X}, t) \quad (1)$$

which is known as the Lagrangian description of motion. Both material and spatial coordinates share the same basis. The displacement  $\mathbf{u}$  is defined as the difference between the spatial and the material coordinates with

$$\mathbf{u}(\mathbf{X}, t) = \mathbf{x}(\mathbf{X}, t) - \mathbf{X}. \quad (2)$$

In non-linear continuum mechanics, the deformation gradient  $\mathbf{F}$  is necessary to map tangents between  $\mathcal{B}_0$  and  $\mathcal{B}$ . It is a second order tensor which is computed using the gradient of the deformation mapping with respect to the material coordinates

$$\mathbf{F} = \frac{\partial \mathbf{x}}{\partial \mathbf{X}} = \frac{\partial(\mathbf{u} + \mathbf{X})}{\partial \mathbf{X}} = \frac{\partial \mathbf{u}}{\partial \mathbf{X}} + \mathbf{I} \quad (3)$$

where  $\mathbf{I}$  denotes the second-order identity tensor. The determinant of the deformation gradient is denoted as the Jacobian  $J = \det(\mathbf{F})$  and is relevant to describe the volume change during the deformation. The general deformation mapping in non-linear kinematics is illustrated in Figure 1. There,  $\mathbf{E}_i$  denote

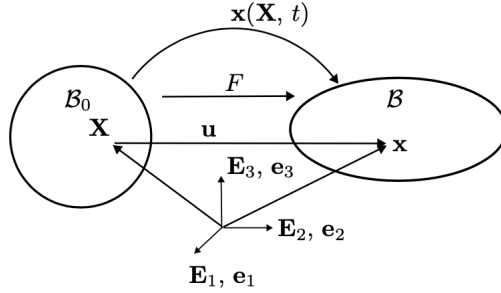


Figure 1: Deformation mapping from the undeformed body  $\mathcal{B}_0$  to the deformed body  $\mathcal{B}$ .

the material basis vectors and  $\mathbf{e}_i$  denote the spatial basis vectors. The following formulas describe the transformation of line, area and volume elements from  $\mathcal{B}_0$  to  $\mathcal{B}$

$$d\mathbf{x} = \mathbf{F}d\mathbf{X} \quad (4)$$

$$\mathbf{n}da = J\mathbf{F}^{-T} \cdot \mathbf{N}dA \quad (5)$$

$$dv = JdV \quad (6)$$

where  $\mathbf{N}$  and  $\mathbf{n}$  denote the outward unit normal vectors in  $\mathcal{B}_0$  and  $\mathcal{B}$  respectively. The existence of  $\mathbf{F}^{-T}$  implies that  $J$  must be non-zero. Also, the transformation of the volume elements demands  $J$  to be non-negative and therefore  $J > 0$ . To describe the non-linear deformation, we utilise different strain measurements.

To account for the geometrical change from  $\mathcal{B}_0$  to  $\mathcal{B}$ , the right Cauchy-Green tensor  $\mathbf{C} = \mathbf{F}^T \mathbf{F}$  is used, whereas the left Cauchy-Green tensor  $\mathbf{b} = \mathbf{F} \mathbf{F}^T$  is used to describe the geometrical change from  $\mathcal{B}$  to  $\mathcal{B}_0$ . Especially for nearly incompressible materials, it is useful to separate the deformation into a volumetric and isochoric part where the latter does not result in any volume change. The isochoric component  $\bar{\mathbf{F}}$  of  $\mathbf{F}$  is defined as

$$\bar{\mathbf{F}} = J^{-\frac{1}{3}} \mathbf{F}. \quad (7)$$

It is evident that  $\det(\bar{\mathbf{F}}) = 1$  meaning that there is no volume change. Using the decomposition of  $\mathbf{F}$ , the isochoric parts of  $\mathbf{C}$  and  $\mathbf{b}$  are obtained as

$$\bar{\mathbf{C}} = \bar{\mathbf{F}}^T \bar{\mathbf{F}} = J^{-\frac{2}{3}} \mathbf{C} \quad \text{and} \quad \bar{\mathbf{b}} = \bar{\mathbf{F}} \bar{\mathbf{F}}^T = J^{-\frac{2}{3}} \mathbf{b}. \quad (8)$$

## 2.2. Governing equations of electromechanics

We now introduce the necessary partial differential equations to model the electro-mechanically coupled behaviour. Additionally, essential boundary conditions are defined to complete the strong problem formulation.

The mechanical deformation of a body is described by the balance of linear momentum with prescribed Dirichlet and Neumann boundary conditions. Neglecting body forces and inertia forces, the following mechanical boundary value problem (BVP) is adopted from [8]

$$\begin{aligned} \operatorname{div}(\boldsymbol{\sigma}) &= \mathbf{0} \quad \text{in } \mathcal{B} \\ \mathbf{u} &= \bar{\mathbf{u}} \quad \text{on } \mathcal{S}_{\mathbf{u}} \\ \boldsymbol{\sigma} \mathbf{n} &= \bar{\mathbf{t}} \quad \text{on } \mathcal{S}_{\mathbf{t}}. \end{aligned} \quad (9)$$

In (9), the Cauchy stress is denoted as  $\boldsymbol{\sigma}$ . Regarding the boundary conditions, the displacement  $\bar{\mathbf{u}}$  and the surface traction force  $\bar{\mathbf{t}}$  are prescribed on the complementary boundary domains  $\mathcal{S}_{\mathbf{u}}$  and  $\mathcal{S}_{\mathbf{t}}$  with  $\mathcal{S}_{\mathbf{u}} \cup \mathcal{S}_{\mathbf{t}} = \partial\mathcal{B}$  and  $\mathcal{S}_{\mathbf{u}} \cap \mathcal{S}_{\mathbf{t}} = \emptyset$ . Neglecting magnetic effects, the spatial propagation of the electric potential  $\varphi$  inside a dielectric elastomer is described by the first Maxwell's equation. We adopt the electric BVP for a dielectric elastomer from [8] with prescribed boundary conditions as

$$\begin{aligned} \operatorname{div}(\mathbf{D}) &= 0 \quad \text{in } \mathcal{B} \\ \varphi &= \bar{\varphi} \quad \text{on } \mathcal{S}_{\varphi} \\ -\mathbf{D} \mathbf{n} &= \bar{\omega} \quad \text{on } \mathcal{S}_{\omega}. \end{aligned} \quad (10)$$

In (10), the spatial electric displacement is denoted as  $\mathbf{D}$ . Regarding the boundary conditions, the electric potential  $\bar{\varphi}$  and the surface charge  $\bar{\omega}$  are prescribed on the complementary boundary domains  $\mathcal{S}_{\varphi}$  and  $\mathcal{S}_{\omega}$  with  $\mathcal{S}_{\varphi} \cup \mathcal{S}_{\omega} = \partial\mathcal{B}$  and  $\mathcal{S}_{\varphi} \cap \mathcal{S}_{\omega} = \emptyset$ .

For the electrical behaviour of the myocardial tissue, we adopt the model derived in [6]. The spatio-temporal evolution of the electric potential inside the

myocardium is defined by the following BVP

$$\begin{aligned} \dot{\varphi} &= \text{div}(\mathbf{q}) + I^\varphi \quad \text{in } \mathcal{B} \cup [t_0, \infty) \\ \varphi_0 &= \varphi(t_0) \quad \text{in } \mathcal{B} \cup \{t_0\} \\ \varphi &= \bar{\varphi} \quad \text{on } \mathcal{S}_\varphi \cup [t_0, \infty) \\ \mathbf{q}\mathbf{n} &= \bar{q} \quad \text{on } \mathcal{S}_q \cup [t_0, \infty). \end{aligned} \quad (11)$$

In (11), the diffusion term  $\text{div}(\mathbf{q})$  defines the spatial propagation of the electric potential  $\varphi$  depending on the spatial flux vector  $\mathbf{q}$ . Additionally, the non-linear source term  $I^\varphi$  defines the generation and evolution of  $\varphi$  over time. For our work, it is computed based on the phenomenological Aliev-Panfilov model introduced by [1]. Regarding the boundary conditions, the electric potential  $\bar{\varphi}$  and the surface flux  $\bar{q}$  are prescribed on the complementary boundary domains  $\mathcal{S}_\varphi$  and  $\mathcal{S}_q$  with  $\mathcal{S}_\varphi \cup \mathcal{S}_q = \partial\mathcal{B}$  and  $\mathcal{S}_\varphi \cap \mathcal{S}_q = \emptyset$ .

### 2.3. Weak formulation

To later apply the numerical methods, the BVPs from Section 2.2 are formulated in a weak description. The Galerkin method is utilised to derive the weak forms of the PDEs from (9)-(11). We introduce the following test functions  $\mathbf{v}_1$  and  $v_2$  and their respective sets  $\mathcal{V}_1$  and  $\mathcal{V}_2$  as follows

$$\begin{aligned} \mathcal{V}_1 &= \{\mathbf{v}_1 \in \mathcal{H}^1 : \mathbf{v}_1 = \mathbf{0} \quad \text{on } \mathcal{S}_u\} \\ \mathcal{V}_2 &= \{v_2 \in \mathcal{H}^1 : v_2 = 0 \quad \text{on } \mathcal{S}_\varphi\} \end{aligned} \quad (12)$$

where  $\mathcal{H}^1$  is the Sobolev-space. The test functions have the property that they vanish on the Dirichlet boundary domain. The weak formulation can be interpreted as the principle of virtual work  $\mathcal{G}$  defined as

$$\mathcal{G} = \mathcal{G}^{\text{int}} - \mathcal{G}^{\text{ext}} = 0 \quad (13)$$

where  $\mathcal{G}^{\text{int}}$  is the internal work and  $\mathcal{G}^{\text{ext}}$  is the external work. The internal work is computed by multiplying the balance equation with the corresponding test function and integrating over the domain  $\mathcal{B}$ . To obtain the external work, the Neumann boundary conditions are also multiplied with the corresponding test function and integrated over the Neumann boundary domain. The spatial weak form for the mechanical problem in (9) results in

$$\mathcal{G}_u = \int_{\mathcal{B}} \boldsymbol{\sigma} : \frac{\partial \mathbf{v}_1}{\partial \mathbf{x}} dv - \int_{\mathcal{S}_t} \mathbf{v}_1 \mathbf{t} da = 0, \quad \forall \mathbf{v}_1 \in \mathcal{V}_1. \quad (14)$$

The spatial weak form for the electrical dielectric elastomer problem from (10) results in

$$\mathcal{G}_{\varphi, \text{die}} = \int_{\mathcal{B}} \frac{\partial v_2}{\partial \mathbf{x}} \mathbf{D} dv - \int_{\mathcal{S}_q} v_2 \bar{q} da = 0, \quad \forall v_2 \in \mathcal{V}_2. \quad (15)$$

Both formulations correspond to the weak forms stated in [8]. The spatial weak form for the electrical myocardial tissue problem from (11) is derived in [7] to

$$\mathcal{G}_{\varphi, \text{myo}} = \int_{\mathcal{B}} [v_2 \dot{\varphi} - \frac{\partial v_2}{\partial \mathbf{x}} \mathbf{q} - v_2 I^\varphi] dv - \int_{\mathcal{S}_q} v_2 \bar{q} da = 0, \quad \forall v_2 \in \mathcal{V}_2. \quad (16)$$

### 3. Constitutive equations

In this section, we summarise the constitutive equations for the dielectric elastomer and the myocardial tissue. These equations relate the solution variables  $\mathbf{u}, \varphi$  to the stress and electrical quantities from (9) - (11) and therefore characterise the coupling behaviour.

#### 3.1. Constitutive equations for the dielectric elastomer

Based on Gauss's law,  $\mathbf{D}$  from (10) is computed as

$$\mathbf{D} = \epsilon \mathbf{E} \quad (17)$$

with the spatial electric field  $\mathbf{E} = -\frac{\partial \varphi}{\partial \mathbf{x}}$  and the dielectric permittivity  $\epsilon$ . The corresponding material electric field is computed by the pull-back operation  $\mathbf{E}_0 = \mathbf{F}^T \mathbf{E}$  with  $\mathbf{E}_0 = -\frac{\partial \varphi}{\partial \mathbf{X}}$ . We adopt the assumption from [8] and neglect the effects of free space surrounding the dielectric for simplistic reasons. Hence, the permittivity of free space  $\epsilon_0$  is set to zero. Accounting for the electro-mechanical coupling,  $\boldsymbol{\sigma}$  is decomposed into an active part  $\boldsymbol{\sigma}^{\text{act}}$  and passive part  $\boldsymbol{\sigma}^{\text{pas}}$ . The electrical polarisation generates  $\boldsymbol{\sigma}^{\text{act}}$  based on [31], while  $\boldsymbol{\sigma}^{\text{pas}}$  is purely mechanical. Additionally, we separate  $\boldsymbol{\sigma}^{\text{pas}}$  into a volumetric part  $\boldsymbol{\sigma}^{\text{vol}}$  and isochoric part  $\boldsymbol{\sigma}^{\text{iso}}$  with  $\boldsymbol{\sigma}^{\text{pas}} = \boldsymbol{\sigma}^{\text{vol}} + \boldsymbol{\sigma}^{\text{iso}}$ . For the dielectric elastomer, we define  $\boldsymbol{\sigma}$  as

$$\boldsymbol{\sigma} = \underbrace{\epsilon[\mathbf{E} \otimes \mathbf{E} - \frac{1}{2}(\mathbf{E}\mathbf{E})\mathbf{I}]}_{\boldsymbol{\sigma}^{\text{act}}} + \underbrace{\frac{\mu}{J}[\mathbf{b} - \mathbf{I}]}_{\boldsymbol{\sigma}^{\text{vol}}} + \underbrace{\frac{\lambda}{J}\ln(J)\mathbf{I}}_{\boldsymbol{\sigma}^{\text{iso}}}. \quad (18)$$

The definition for  $\boldsymbol{\sigma}^{\text{act}}$  is adopted from [31] and the definition of  $\boldsymbol{\sigma}^{\text{pas}}$  is adopted from [2]. The parameters  $\mu$  and  $\lambda$  denote the first and second Lamé's parameter and are material-dependent. The passive isotropic behaviour is described by the Neo-Hookean model for the compressible case.

#### 3.2. Constitutive equations for the myocardium

As mentioned in Section 2.2, the term  $I^\varphi$  from (11) is computed based on the procedure in [6] using the Aliev-Panfilov model from [1]. For further information regarding the explicit computation of  $I^\varphi$ , the reader is referred to those works. The flux vector  $\mathbf{q}$  is defined in [6, 20] as

$$\mathbf{q} = d \frac{\partial \varphi}{\partial \mathbf{x}} = -d \mathbf{E} \quad (19)$$

where  $d$  is the scalar conductivity. For this work, we assume isotropy for the spatial propagation of  $\varphi$ . Hence, a scalar representation of the conductivity is sufficient. This assumption is made to reduce the complexity of the numerical implementation. Similar to the dielectric elastomer, we decompose  $\boldsymbol{\sigma}$  of the

myocardial tissue into  $\boldsymbol{\sigma}^{\text{act}}$  and  $\boldsymbol{\sigma}^{\text{pas}}$  with an additional subdivision in  $\boldsymbol{\sigma}^{\text{vol}}$  and  $\boldsymbol{\sigma}^{\text{iso}}$  with  $\boldsymbol{\sigma}^{\text{pas}} = \boldsymbol{\sigma}^{\text{vol}} + \boldsymbol{\sigma}^{\text{iso}}$

$$\boldsymbol{\sigma} = \underbrace{\frac{1}{J}T(\varphi)\mathbf{f} \otimes \mathbf{f}}_{\boldsymbol{\sigma}^{\text{act}}} + \underbrace{\kappa(J-1)\mathbf{I}}_{\boldsymbol{\sigma}^{\text{vol}}} + \underbrace{\bar{\boldsymbol{\sigma}} : \mathbb{P}}_{\boldsymbol{\sigma}^{\text{iso}}} \quad (20)$$

with the active fibre tension  $T(\varphi)$  in the fibre direction  $\mathbf{f} = \mathbf{F}\mathbf{f}_0$ , the modified Cauchy stress  $\bar{\boldsymbol{\sigma}}$  and the isochoric fourth-order projection tensor  $\mathbb{P} = \mathbb{I}^{\text{sym}} - \frac{1}{3}\mathbf{I} \otimes \mathbf{I}$  in which  $\mathbb{I}^{\text{sym}}$  is the symmetric fourth-order identity tensor defined as  $\mathbb{I}_{ijkl}^{\text{sym}} = \frac{1}{2}(\delta_{ik}\delta_{jl} + \delta_{il}\delta_{jk})$ . The material directions  $\mathbf{f}_0$  and  $\mathbf{s}_0$  define the undeformed fibre and sheet orientations in the myocardium as illustrated in Figure 2. To compute

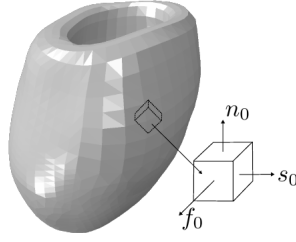


Figure 2: Anisotropic model of the myocardium. The orientation of a single myocardial cell is defined by a orthonormal  $\mathbf{f}_0 - \mathbf{s}_0 - \mathbf{n}_0$ -basis. There,  $\mathbf{f}_0$  denotes the fibre direction,  $\mathbf{s}_0$  the sheet direction and  $\mathbf{n}_0$  the normal direction in material configuration.

$\boldsymbol{\sigma}^{\text{act}}$ ,  $T(\varphi)$  is evaluated based on the definition from [23]

$$\dot{T} = a(\varphi)[k_T(\varphi - \varphi_r) - T] \quad (21)$$

with the control parameter  $k_T$ , the resting potential  $\varphi_r$  and the switch function  $a(\varphi)$ . The parameter  $k_T$  controls the amplitude of  $\boldsymbol{\sigma}^{\text{act}}$ . The switch function is a smoothed form of the Heaviside step function. It is explicitly defined as

$$a(\varphi) = a_0 + (a_\infty - a_0)\exp[-\exp(-\xi(\varphi - \bar{\varphi}))] \quad (22)$$

where  $\bar{\varphi}$  is the phase shift and  $a_0$  and  $a_\infty$  are limiting parameters. In contrast to [7], the following inequality  $a_0 > a_\infty$  must hold. This relation is proposed in [4] in order to achieve a temporal delay between the peak of  $\boldsymbol{\sigma}^{\text{act}}$  and the amplitude of  $\varphi$ . The function approaches  $a_\infty$  for  $\varphi < \bar{\varphi}$  and  $a_0$  for  $\varphi > \bar{\varphi}$ . The parameter  $\xi$  controls the transition rate. A backward Euler scheme is used to compute  $T(\varphi)$  iteratively.

In (20),  $\boldsymbol{\sigma}^{\text{vol}}$  is defined by the material-dependent bulk modulus  $\kappa$  and  $\boldsymbol{\sigma}^{\text{iso}}$  is computed based on the Holzapfel-Ogden model. This model was introduced in [9, 10] and expanded in [5] to account for incompressible material. To formulate



$\bar{\sigma}$ , we first state the Holzapfel-Ogden strain energy function  $\Psi$  from [5]

$$\begin{aligned}\Psi &= \Psi^{\text{iso}} + \Psi^{\text{aniso}} = \Psi^{\text{iso}} + \Psi^f + \Psi^s + \Psi^{fs} \quad \text{with} \\ \Psi^{\text{iso}} &= \frac{a}{2b} \exp[b(\bar{I}_1 - 3)], \\ \Psi^f &= \frac{a_f}{2b_f} [\exp[b_f(\bar{I}_f - 1)^2] - 1], \\ \Psi^s &= \frac{a_s}{2b_s} [\exp[b_s(\bar{I}_s - 1)^2] - 1] \quad \text{and} \\ \Psi^{fs} &= \frac{a_{fs}}{2b_{fs}} [\exp[b_{fs}(\bar{I}_{fs})^2] - 1].\end{aligned}\tag{23}$$

The energy is formulated in terms of the isochoric invariants  $\bar{I}_1$ ,  $\bar{I}_f$ ,  $\bar{I}_s$  and  $\bar{I}_{fs}$  and independent material parameters  $a$ ,  $b$ ,  $a_f$ ,  $b_f$ ,  $a_s$ ,  $b_s$ ,  $a_{fs}$  and  $b_{fs}$ . The invariants are as

$$\begin{aligned}\bar{I}_1 &= \text{tr}(\bar{\mathbf{b}}), \quad \bar{I}_f = \text{tr}(\bar{\mathbf{f}} \otimes \bar{\mathbf{f}}), \\ \bar{I}_s &= \text{tr}(\bar{\mathbf{s}} \otimes \bar{\mathbf{s}}) \quad \text{and} \quad \bar{I}_{fs} = \text{tr}[(\bar{\mathbf{f}} \otimes \bar{\mathbf{s}})^{\text{sym}}]\end{aligned}\tag{24}$$

with the spatial isochoric directions  $\bar{\mathbf{f}} = \bar{\mathbf{F}}\mathbf{f}_0$  and  $\bar{\mathbf{s}} = \bar{\mathbf{F}}\mathbf{s}_0$ . We adopt the explicit formulation of  $\bar{\sigma}$  from [5] as

$$\begin{aligned}\bar{\sigma} &= \frac{1}{J} \left[ 2 \frac{\partial \Psi^{\text{iso}}}{\partial \bar{I}_1} \bar{\mathbf{b}} + 2 \frac{\partial \Psi^f}{\partial \bar{I}_f} \bar{\mathbf{f}} \otimes \bar{\mathbf{f}} + 2 \frac{\partial \Psi^s}{\partial \bar{I}_s} \bar{\mathbf{s}} \otimes \bar{\mathbf{s}} \right. \\ &\quad \left. + \frac{\partial \Psi^{fs}}{\partial \bar{I}_{fs}} (\bar{\mathbf{f}} \otimes \bar{\mathbf{f}} + \bar{\mathbf{s}} \otimes \bar{\mathbf{s}}) \right].\end{aligned}\tag{25}$$

$\sigma^{\text{iso}}$  is then computed by a double contraction between  $\bar{\sigma}$  and  $\mathbb{P}$ , see (20).

#### 4. Numerical solution procedure using S-FEM

In this section, we summarise the numerical approximations of the governing equations and solution variables. First some fundamentals of the FEM theory are introduced which serve as basics for S-FEM. Then, the approximation scheme using S-FEM is presented. To implement the numerical solution scheme, the discretisation and linearisation of the spatial weak formulations is described. We mainly adopt the descriptions from [30] regarding the non-linear FEM and the descriptions from [15] regarding the S-FEM formulation.

##### 4.1. Finite element method

In standard FEM, the original geometry  $\mathcal{B}$  is subdivided into so-called finite elements  $\mathcal{B}^e$ . The elements are connected to each other by their nodes and form an approximation geometry  $\mathcal{B}^h$ , such that  $\mathcal{B} \approx \mathcal{B}^h = \bigcup_{e=1}^{N_{el}} \mathcal{B}^e$ . There,

$N_{el}$  is the total number of  $\mathcal{B}^e$ . The element-wise solution variables  $\mathbf{u}^e$ ,  $\varphi^e$  are approximated on each  $\mathcal{B}^e$  as

$$\mathbf{u}^e = \sum_{a=1}^{n_n} \mathbf{u}^a N^a \quad \text{and} \quad (26)$$

$$\varphi^e = \sum_{a=1}^{n_n} \varphi^a N^a \quad (27)$$

where  $n_n$  is the number of element nodes and  $N^a$  is the nodal shape function. The index  $a$  denotes the local node number. Each quantity is evaluated at  $a$  and weighted by the corresponding  $N^a$ . Following the Galerkin method, the element-wise test functions  $\mathbf{v}_1^e$ ,  $v_2^e$  can also be approximated by the same shape functions as

$$\mathbf{v}_1^e = \sum_{a=1}^{n_n} \mathbf{v}_1^a N^a \quad \text{and} \quad (28)$$

$$v_2^e = \sum_{a=1}^{n_n} v_2^a N^a. \quad (29)$$

For the discretisation of the weak forms in Section 2.3, the test function gradients also need to be computed element-wise. Only the shape functions are affected by the gradient operator. Therefore, the test function gradients result in

$$\frac{\partial \mathbf{v}_1^e}{\partial \mathbf{x}} = \sum_{a=1}^{n_n} \mathbf{v}_1^a \otimes \frac{\partial N^a}{\partial \mathbf{x}} \quad \text{and} \quad (30)$$

$$\frac{\partial v_2^e}{\partial \mathbf{x}} = \sum_{a=1}^{n_n} v_2^a \frac{\partial N^a}{\partial \mathbf{x}}. \quad (31)$$

Additionally, we can approximate the element-wise deformation gradient  $\mathbf{F}^e$  and electric field  $\mathbf{E}^e$  as

$$\begin{aligned} \mathbf{F}^e &= \sum_{a=1}^{n_n} \mathbf{u}^a \otimes \frac{\partial N^a}{\partial \mathbf{X}} + \mathbf{I} \quad \text{and} \\ \mathbf{E}^e &= \sum_{a=1}^{n_n} \varphi^a (\mathbf{F}^e)^{-T} \frac{\partial N^a}{\partial \mathbf{X}}. \end{aligned} \quad (32)$$

#### 4.2. Smoothed finite element method

The basic concept of S-FEM is to apply a smoothing operation on the gradients over defined SDs, according to [14]. The spatial body  $\mathcal{B}$  is subdivided into non-overlapping cells such that  $\mathcal{B} \approx \bigcup_{k=1}^{N_s} \mathcal{B}^k$ . There,  $\mathcal{B}^k$  is a SD and  $N_s$  is the total number of SDs. The resulting SD mesh is over-layered on an initial FEM mesh. This work focuses on two main smoothing methods in 3D, FS-FEM presented in [24] and NS-FEM presented in [25]. In FS-FEM, the smoothing

domain is created around the connecting faces of neighbouring elements. First, the connecting faces between two elements is identified. Then, the nodes of each face are connected with the respective element centroids to form the face-based SDs. For elements on the boundary, the nodes on the boundary face are connected to the centroid of the boundary element. The total number of SDs in FS-FEM is equal to the number of faces in the FEM mesh. In NS-FEM, each SD is created around the connecting node of adjacent elements. For each node, the connecting elements are identified. Then, the mid-points of the edges connected to the node, the connected element centroids and the centroids of the connected faces together with the node itself form the node-based SD. The volume of the node-based SD depends on the number of adjacent elements. The total number of node-based SDs is equal to the number of nodes in the FEM mesh. In this work, the SDs are constructed based on four node tetrahedral elements. In Figure 3, the resulting SDs are depicted for NS-FEM and FS-FEM. In [14], the

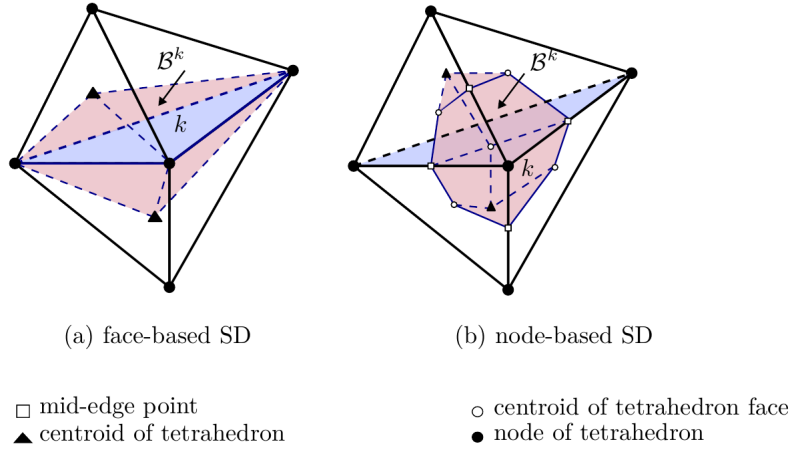


Figure 3: SDs on an initial 3D TET mesh where  $\mathcal{B}^k$  for FS-FEM is constructed around a connecting face  $k$  in (a) and for NS-FEM,  $\mathcal{B}^k$  is constructed around a connecting node  $k$  in (b) (adopted from [19]).

following smoothing function  $\Phi(\mathbf{X})$  is introduced

$$\Phi(\mathbf{X}) = \begin{cases} \frac{1}{V^k} & \text{if } \mathbf{X} \in \mathcal{B}^k \\ 0 & \text{else} \end{cases} \quad (33)$$

where  $V^k$  is the volume of the smoothing domain with  $V^k = \int_{\mathcal{B}^k} dV$ . Additionally,  $\Phi(\mathbf{X})$  also satisfies the positivity and unity conditions

$$\Phi(\mathbf{X}) \geq 0 \quad \text{and} \quad \int_{\mathcal{B}^k} \Phi(\mathbf{X}) dV = 1. \quad (34)$$

The original idea behind S-FEM was to apply  $\Phi(\mathbf{X})$  to the element-wise strains connected to the respective SD leading to a smoothed deformation gradient.

Using (33), the smoothed deformation gradient  $\mathbf{F}^k$  can be derived from

$$\mathbf{F}^k = \int_{\mathcal{B}^k} \frac{\partial \mathbf{u}}{\partial \mathbf{X}} \Phi(\mathbf{X}) dV + \mathbf{I} = \frac{1}{V^k} \int_{\mathcal{B}^k} \frac{\partial \mathbf{u}}{\partial \mathbf{X}} dV + \mathbf{I}. \quad (35)$$

The SDs around the faces or nodes consist of contributions from the adjacent elements. Therefore, (35) can be rewritten into

$$\mathbf{F}^k = \frac{1}{4V^k} \sum_{e=1}^{n_k} \frac{\partial \mathbf{u}}{\partial \mathbf{X}} V^e + \mathbf{I} \quad (36)$$

where  $n_k$  is the number of adjacent tetrahedrons  $\mathcal{B}^e$  around node  $k$  or face  $k$  and  $V^e$  is the volume of each  $\mathcal{B}^e$ . With further transformations and based on [19], (36) results in

$$\mathbf{F}^k = \frac{1}{4V^k} \sum_{e=1}^{n_k} \sum_{a=1}^{n_n} \mathbf{u}^a \otimes \frac{\partial N^a}{\partial \mathbf{X}} V^e + \mathbf{I} \quad (37)$$

where  $n_n=4$  because of the use of tetrahedral elements. Due to the electro-mechanical coupling, the gradient smoothing operation also affects the electric field  $\mathbf{E}$  which results in a smoothed spatial electric field  $\mathbf{E}^k$ . Adopting the same steps used for the derivation of (37), the explicit approximation of  $\mathbf{E}^k$  results in

$$\mathbf{E}^k = -\frac{1}{4V^k} \sum_{e=1}^{n_k} \underbrace{\sum_{a=1}^{n_n} \varphi^a(\mathbf{F}^e)^{-T} \frac{\partial N^a}{\partial \mathbf{X}} V^e}_{-\mathbf{E}^e}. \quad (38)$$

Additionally to the gradient smoothing, the solution variables are also affected by the smoothing operation. The smoothed solutions  $\mathbf{u}^k$ ,  $\varphi^k$  correspond to the solution on the SD. Applying  $\Phi(\mathbf{X})$  on  $\mathbf{u}$  and  $\varphi$  results in

$$\mathbf{u}^k = \frac{1}{4V^k} \sum_{e=1}^{n_k} \underbrace{\sum_{a=1}^4 \mathbf{u}^a N^a V^e}_{\mathbf{u}^e} \quad \text{and} \quad (39)$$

$$\varphi^k = \frac{1}{4V^k} \sum_{e=1}^{n_k} \underbrace{\sum_{a=1}^4 \varphi^a N^a V^e}_{\varphi^e}. \quad (40)$$

To complete the approximations, we also state the smoothed test functions  $\mathbf{v}_1^k$ ,  $v_2^k$  as

$$\mathbf{v}_1^k = \frac{1}{4V^k} \sum_{e=1}^{n_k} \underbrace{\sum_{a=1}^{n_n} \mathbf{v}_1^a N^a}_{\mathbf{v}_1^e} V^e \quad \text{and} \quad (41)$$

$$v_2^k = \frac{1}{4V^k} \sum_{e=1}^{n_k} \underbrace{\sum_{a=1}^{n_n} v_2^a N^a}_{v_2^e} V^e. \quad (42)$$

The smoothed test function gradients then result in

$$\frac{\partial \mathbf{v}_1^k}{\partial \mathbf{x}} = \frac{1}{4V^k} \sum_{e=1}^{n_k} \underbrace{\sum_{a=1}^{n_n} \mathbf{v}_1^a \otimes \frac{\partial N^a}{\partial \mathbf{x}}}_{\partial \mathbf{v}_1^e / \partial \mathbf{x}} V^e \quad \text{and} \quad (43)$$

$$\frac{\partial v_2^k}{\partial \mathbf{x}} = \frac{1}{4V^k} \sum_{e=1}^{n_k} \underbrace{\sum_{a=1}^{n_n} v_2^a \frac{\partial N^a}{\partial \mathbf{x}}}_{\partial v_2^e / \partial \mathbf{x}} V^e. \quad (44)$$

We observe, that the smoothed quantities are just the averaged values of the corresponding element-wise quantities over all elements that are connected to the SD.

#### 4.3. Spatial discretisation

We now describe the spatial discretisation of the electro-mechanically coupled problem using the S-FEM approximations from Section 4.2. The procedure is analogue to standard FEM. First, the mechanical problem defined by the weak form in (14) is discretised. The local residual  $\mathbf{R}_u^a$  of the SD is obtained by inserting (43) into (14). We adopt the assumptions from [8] and neglect the surface traction force for this work. Therefore,  $\mathbf{R}_u^a$  results in

$$\mathbf{R}_u^a = \int_{B^k} \boldsymbol{\sigma}^k \nabla N^a dv = \mathbf{0} \quad (45)$$

where  $\boldsymbol{\sigma}^k$  is the smoothed Cauchy stress computed in terms of  $\mathbf{F}^k$  and  $\mathbf{E}^k$ . Depending on the chosen material model,  $\boldsymbol{\sigma}^k = \boldsymbol{\sigma}(\mathbf{F}^k, \mathbf{E}^k)$  is either derived from (18) or (20). For sake of compactness, we denote the spatial shape function gradient as  $\nabla N^a = \frac{\partial N^a}{\partial \mathbf{x}}$  from now on.

The local residual for the dielectric elastomer problem  $R_{\varphi, \text{die}}^a$  is derived from (15). We again adopt the assumption from [8] and neglect the surface charge. Therefore,  $R_{\varphi, \text{die}}^a$  results in

$$R_{\varphi, \text{die}}^a = \int_{B^k} \mathbf{D}^k \nabla N^a dv = 0 \quad (46)$$

where the smoothed electric displacement  $\mathbf{D}^k = \mathbf{D}(\mathbf{E}^k)$  is computed from (17). For the myocardial tissue, the weak form from (16) is discretised into the local residual  $R_{\varphi, \text{myo}}^a$ . Based on the FEM discretisation in [7] and neglecting the surface flux,  $R_{\varphi, \text{myo}}^a$  results in

$$R_{\varphi, \text{myo}}^a = \int_{\mathcal{B}^k} [N^a \frac{\varphi^k - \varphi_n^k}{\Delta t} - \nabla N^a \mathbf{q}^k dv - N^a I^{\varphi, k}] dv = 0. \quad (47)$$

In (47), the time derivative of  $\varphi^k$  is approximated by the finite difference  $\frac{\varphi^k - \varphi_n^k}{\Delta t}$  where  $n$  denotes the previous time and  $\Delta t$  the time increment. The smoothed flux  $\mathbf{q}^k = \mathbf{q}(\mathbf{E}^k)$  is computed from (19) and the smoothed source term  $I^{\varphi, k} = I^{\varphi}(\varphi^k)$  is computed from the Aliev-Panfilov model employed in [6].

#### 4.4. Linearisation and iterative solution

The local residual  $\mathbf{R}^a = (\mathbf{R}_{\mathbf{u}}^a, R_{\varphi}^a)^T$  consists of the mechanical part  $\mathbf{R}_{\mathbf{u}}^a$  and the electrical part  $R_{\varphi}^a$ . Depending on the problem, either (46) or (47) are used for  $R_{\varphi}^a$ . To solve the non-linear system of equations in  $\mathbf{R}^a$ , the Newton-Raphson method is employed. For the general theory behind this numerical scheme, the reader is referred to [30]. Applying the iterative method leads to the following tangent matrices  $\mathbf{K}_{\mathbf{u}\mathbf{u}}^{ab}$ ,  $\mathbf{K}_{\mathbf{u}\varphi}^{ab}$ ,  $\mathbf{K}_{\varphi\mathbf{u}}^{ab}$  and  $\mathbf{K}_{\varphi\varphi}^{ab}$  which are given by

$$\begin{aligned} \mathbf{K}_{\mathbf{u}\mathbf{u}}^{ab} &= -\frac{\partial \mathbf{R}_{\mathbf{u}}^a}{\partial \mathbf{u}^b}, & \mathbf{K}_{\mathbf{u}\varphi}^{ab} &= -\frac{\partial \mathbf{R}_{\mathbf{u}}^a}{\partial \varphi^b}, \\ \mathbf{K}_{\varphi\mathbf{u}}^{ab} &= -\frac{\partial R_{\varphi}^a}{\partial \mathbf{u}^b} & \text{and} & \quad \mathbf{K}_{\varphi\varphi}^{ab} = -\frac{\partial R_{\varphi}^a}{\partial \varphi^b}. \end{aligned} \quad (48)$$

Combining the individual tangents leads to the local tangent stiffness matrix  $\mathbf{K}^{ab}$ . For the dielectric elastomer, we linearise and solve (45) and (46). The individual parts from (48) result in

$$\mathbf{K}_{\mathbf{u}\mathbf{u}}^{ab} = \int_{\mathcal{B}^k} \nabla N^a \mathbb{C}_{\mathbf{u}\mathbf{u}} \nabla N^b dv, \quad (49)$$

$$\mathbf{K}_{\mathbf{u}\varphi}^{ab} = \int_{\mathcal{B}^k} \nabla N^a \mathbb{C}_{\mathbf{u}\varphi} \nabla N^b dv, \quad (50)$$

$$\mathbf{K}_{\varphi\mathbf{u}}^{ab} = \int_{\mathcal{B}^k} \nabla N^a \mathbb{C}_{\varphi\mathbf{u}} \nabla N^b dv \quad \text{and} \quad (51)$$

$$\mathbf{K}_{\varphi\varphi}^{ab} = \int_{\mathcal{B}^k} \nabla N^a \mathbb{C}_{\varphi\varphi} \nabla N^b dv. \quad (52)$$

For the coupled myocardial problem, we linearise and solve (45) and (47). The structure of  $\mathbf{K}_{\mathbf{u}\mathbf{u}}^{ab}$ ,  $\mathbf{K}_{\mathbf{u}\varphi}^{ab}$  and  $\mathbf{K}_{\varphi\mathbf{u}}^{ab}$  does not change. Because of the additional terms in  $R_{\varphi, \text{myo}}^a$ , the stiffness  $\mathbf{K}_{\varphi\varphi}^{ab}$  results in

$$\mathbf{K}_{\varphi\varphi}^{ab} = \int_{\mathcal{B}^k} [N^a \frac{1}{\Delta t} N^b + \nabla N^a \mathbb{C}_{\varphi\varphi} \nabla N^b - N^a \frac{\partial I^{\varphi, k}}{\partial \varphi^k} N^b] dv \in \mathbb{R}. \quad (53)$$

The explicit formulations of the sensitivities  $\mathbb{C}_{\mathbf{u}\mathbf{u}}$ ,  $\mathbb{C}_{\mathbf{u}\varphi}$ ,  $\mathbb{C}_{\varphi\mathbf{u}}$  and  $\mathbb{C}_{\varphi\varphi}$  differ between the dielectric elastomer and the myocardial tissue. Because the integration is done over the SD, the sensitivities are computed based on  $\mathbf{F}^k$  and  $\mathbf{E}^k$ . We adopt the procedure from [8] for the dielectric elastomer and from [7] for the myocardium. The computation for the smoothed sensitivities is analogous to the element-wise ones.

#### 4.5. Implementation

As simulation environment, we choose the commercial computer aided engineering software Abaqus offering custom user element implementation via a subroutine UEL. For a user-defined mesh, the UEL computes and returns the local residuals  $\mathbf{R}^a$  and the tangent stiffness matrices  $\mathbf{K}^{ab}$ . The Abaqus solver then assembles the local quantities into a global system of equations and computes the node-wise solutions. For this work, we created UELs for linear FEM on a TET mesh, FS-FEM on a face-based SD mesh, NS-FEM on a node-based SD mesh and FSNS-FEM on a combined face-based SD mesh and a node-based SD mesh. For FSNS-FEM, the volumetric quantities are evaluated on the node-based SD mesh and the remaining on the face-based SD mesh. The SD meshes are created on top of an initial TET mesh. We adopted the UEL code structure from [28] and implemented the computation of the smoothed kinematic and constitutive quantities based on [19] for the dielectric elastomer and the myocardial tissue. In Table 1, we summarise the numerical methods used for the dielectric elastomer problem. For each numerical method, the table identifies on which element or SD,  $\boldsymbol{\sigma}^{\text{act}}$ ,  $\boldsymbol{\sigma}^{\text{vol}}$ ,  $\boldsymbol{\sigma}^{\text{iso}}$  and  $\mathbf{D}$  are computed to construct the residuals. The corresponding stiffness matrices are also computed on the respective element or SD. In the same manner, we summarise the numerical

| method/discretisation | TET                               | face-based SD  | node-based SD                      |
|-----------------------|-----------------------------------|--|------------------------------------|
| FEM                   | $\boldsymbol{\sigma}, \mathbf{D}$ |  |                                    |
| FS-FEM                |                                   | $\boldsymbol{\sigma}, \mathbf{D}$  |                                    |
| NS-FEM                |                                   |  | $\boldsymbol{\sigma}, \mathbf{D}$  |
| FSNS-FEM              |                                   | $\boldsymbol{\sigma}^{\text{act}}, \boldsymbol{\sigma}^{\text{iso}}, \mathbf{D}$ | $\boldsymbol{\sigma}^{\text{vol}}$ |

Table 1: For each numerical method, we list the location where the Cauchy stress  $\boldsymbol{\sigma}$  and the electric displacement  $\mathbf{D}$  are being evaluated for the dielectric elastomer implementation. The corresponding sensitivities necessary for the Newton-Raphson method are calculated on the same location.

methods for the myocardial tissue problem in Table 2. In contrast to (47), the source term  $I^{k,\varphi}$  is not computed inside the SD but on the TET mesh for each method. Therefore,  $I^{k,\varphi} = I^\varphi$  because the smoothing operation does not effect the source term. The temporal evolution of the electric potential is the same for each numerical method. We note, that the smoothing of  $I^\varphi$  should be included in future implementations for an accurate computation of the local residuals.

| method/discretisation | TET                             | face-based SD  | node-based SD         |
|-----------------------|---------------------------------|--|-----------------------|
| FEM                   | $\sigma, \mathbf{q}, I^\varphi$ |  |                       |
| FS-FEM                | $I^\varphi$                     | $\sigma, \mathbf{q}$                                   |                       |
| NS-FEM                | $I^\varphi$                     |  | $\sigma, \mathbf{q}$  |
| FSNS-FEM              | $I^\varphi$                     | $\sigma^{\text{act}}, \sigma^{\text{iso}}, \mathbf{q}$ | $\sigma^{\text{vol}}$ |

Table 2: For each numerical method, we list the location where the Cauchy stress  $\sigma$ , the electric flux  $\mathbf{q}$  are being evaluated for the myocardial implementation. The corresponding sensitivities necessary for the Newton-Raphson method are calculated on the same location. The source term  $I^\varphi$  is computed on the initial TET mesh for each method.

## 5. Numerical examples

In this section, the implementations of the numerical methods are tested for benchmark problems and evaluated with respect to their accuracy and simulation time. A simple cube representing a DEA and myocardial tissue serves as test geometry.

### 5.1. Coupled DEA cube

For the dielectric elastomer problem, we test the implementations of the numerical methods on a simple electro-mechanically coupled cube with passive Neo-Hookean material. The edge length is set to  $l = 10$  mm. We define 256 nodes within the geometry which results in a discretisation into 1050 TET elements for FEM (TET-FEM), 2250 face-based SDs for FS-FEM and 256 node-based SDs for NS-FEM. For FSNS-FEM, 256 node-based SDs are over-layered on top of 2250 face-based SDs. The mechanical and electrical material parameters are summarised in Table 3. The cube is fixed in three directions preventing a rigid

| $\mu$ [kPa] | $\lambda$ [kPa] | $\epsilon$ [Fmm <sup>-2</sup> ] |
|-------------|-----------------|---------------------------------|
| 2000        | 666.67          | 1                               |

Table 3: Material parameters for the dielectric elastomeric cube.

body motion. The cube is actuated by an external potential which results in contraction. The external potential is partially applied on the cube's front face and varies over time. It is defined as an electrical boundary condition  $\bar{\varphi}(t)$ . The potential on the opposite face is fixed at  $\bar{\varphi}_0 = 0$  mV. The simulation setup is depicted in Figure 4. There,  $\mathcal{S}$  defines the excitation surface on which  $\bar{\varphi}(t)$  is applied. The contraction simulation is carried out in two steps. First,  $\bar{\varphi}(t)$  is linearly increased from 0 mV to 100 mV over a time span of 50 ms. This leads to an indentation on  $\mathcal{S}$ . We denote the first step as the loading step. Second,  $\bar{\varphi}(t)$  is linearly decreased back to 0 mV over a time span of 50 ms. The cube then deforms back to its initial state. We denote the second step as unloading step. Additionally, a reference simulation on a hexahedral mesh (HEX) with 125 elements is conducted to evaluate the accuracy of the numerical methods. We will denote the reference simulation as HEX-FEM. In Figure 5, snapshots



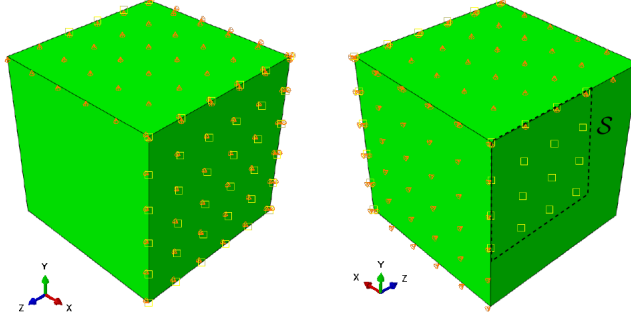


Figure 4: Location of the mechanical (orange cones) and electrical (yellow squares) boundary conditions for the DEA cube simulation. The displacement of the nodes on the excited surface  $S$  are later evaluated.

taken in Abaqus at  $t = 50$  ms for each numerical method are depicted showing the displacement magnitude  $\|\mathbf{u}\|$ . The partial indentations of the excited faces are clearly visible. We further evaluate the averaged displacement magnitude

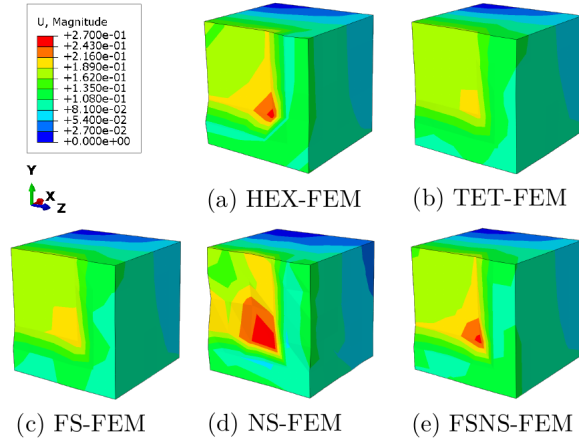


Figure 5: Snapshot taken at  $t = 50$  ms in Abaqus of the displacement magnitude  $\|\mathbf{u}\|$  in mm for each numerical method.

on  $S$  over time. Due to the symmetry in the electrical loading and unloading, we only show the results for the loading step. The deformation curves for each numerical method are depicted in Figure 6. We observe that the simulations using TET-FEM and FS-FEM yield deformations that are below the reference solution. This indicates an overestimated stiffness for both methods. The simulation using NS-FEM yields a deformation curve which is above the reference solution. This indicates an overestimated softness which corresponds to the limitations of NS-FEM stated in [27]. The simulation using FSNS-FEM

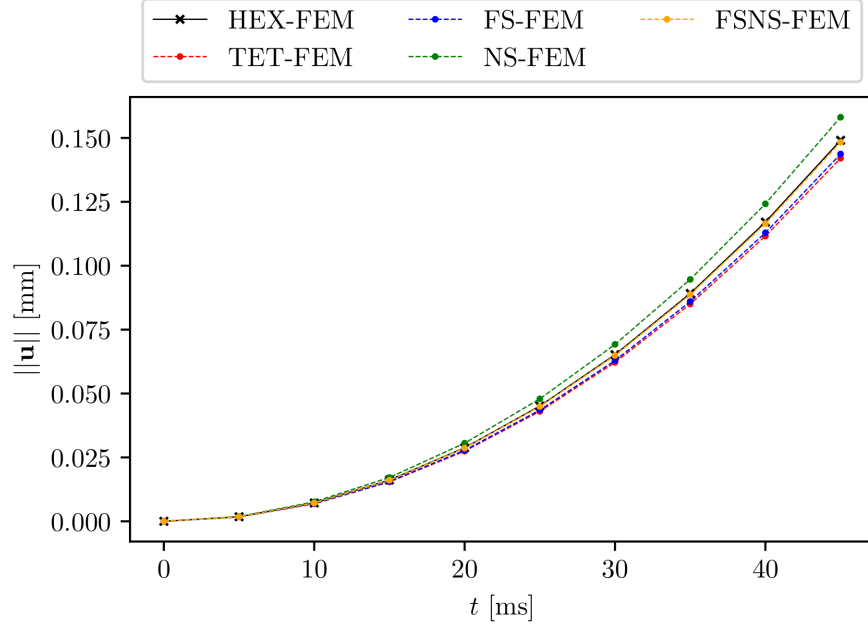


Figure 6: Averaged displacement magnitude  $\|u\|$  on excited surface  $\mathcal{S}$  during the loading step  $t \in [0, 50]$  ms for each method.

returns results which are nearly identical to the reference solution indicating a high accuracy. For each S-FEM and TET-FEM we compute the relative error averaged over all  $n_t$  time steps with

$$\overline{e_r} = \frac{1}{n_t} \sum_{i=1}^{n_t} \left| 1 - \frac{\|u\|_i}{\|u\|_i^{\text{ref}}} \right| \quad (54)$$

where  $\|u\|_i$  is the of the displacement magnitude at time step  $i$  of the respective method depicted in Figure 6 and  $\|u\|_i^{\text{ref}}$  is the displacement magnitude of the HEX-FEM solution. The results are listed in Table 4 together with the total central processing unit (CPU) times of each S-FEM and TET-FEM simulation. The NS-FEM simulation runs the shortest with a CPU time of 11 s but pro-

| method   | $\overline{e_r}$ [-] | CPU time [s] |
|----------|----------------------|--------------|
| TET-FEM  | 0.047                | 299.9        |
| FS-FEM   | 0.036                | 39.3         |
| NS-FEM   | 0.061                | 11.0         |
| FSNS-FEM | 0.005                | 61.7         |

Table 4: Mean relative error  $\overline{e_r}$  over simulation time with respect to HEX-FEM and total CPU time for each numerical method.

duces results with the highest error with  $\bar{\epsilon}_r = 6.1\%$ . The remaining methods return sufficiently accurate solutions where the error is below 5%. The simulation using TET-FEM runs the longest with a CPU time of around 300 s which is nearly five times higher than the second longest simulation using FSNS-FEM. This observation shows that the use of linear TET elements is inefficient compared to FS-FEM and FSNS-FEM. The FSNS-FEM simulation has the smallest error with  $\bar{\epsilon}_r = 0.5\%$  with a total CPU time of 61.7 ms which is nearly five times shorter than for TET-FEM but still the second longest simulation. The FS-FEM simulation runs second shortest with a total CPU time of 39.3 s and an error of  $\bar{\epsilon}_r = 3.6\%$ . But the observation in Figure 6 shows an overestimation of the stiffness over time when using FS-FEM but FSNS-FEM. Therefore, we conclude that FSNS-FEM is the most suitable method to simulate the dielectric elastomer problem because it overcomes the overly-stiff behaviour of TET elements without overestimating the softness resulting in the most accurate solution with an error below 1% which is a sufficient trade-off for the longer CPU time.

### 5.2. Myocardial tissue sample

For this numerical example, the cube geometry represents a section of the myocardium over the whole thickness of the left ventricle where the front face represent the epicardium and the back face represent the endocardium. For the simulation, we use the same discretisation as for the dielectric problem. In summary, 256 nodes are defined inside the cube, resulting in a mesh consisting of 1050 TET elements for TET-FEM, 2250 face-based SDs for FS-FEM, 256 node-based SDs for NS-FEM, and a combination of face-based/node-based SDs for FSNS-FEM. To mimic the orthotropic behaviour of the myocardium based on the Holzapfel-Ogden model, given in (23), we implement rule-based local fibre, sheet and sheet-normal directions,  $\mathbf{f}_0$ ,  $\mathbf{s}_0$  and  $\mathbf{n}_0$ , respectively. Globally, the fibres are aligned by  $+60^\circ$  on the epicardium (front face in Figure 7) and  $-60^\circ$  on the endocardium (front face in Figure 7). The rotation of the fibres throughout the myocardium is fairly smooth. For a TET mesh, each element  $e$  gets a local  $\mathbf{f}_0^e - \mathbf{s}_0^e - \mathbf{n}_0^e$  coordinate system assigned. For S-FEM, the coordinate system is assigned to each SD. Therefore, the directional vectors are also smoothed. We adopt the computation of the smoothed directions  $\mathbf{f}_0^k - \mathbf{s}_0^k - \mathbf{n}_0^k$  from [19]. There, they are derived by averaging the  $\mathbf{f}_0^e - \mathbf{s}_0^e - \mathbf{n}_0^e$  from each element connected to either face  $k$  or node  $k$  with

$$\mathbf{f}_0^k = \frac{1}{n_k} \sum_{e=1}^{n_k} \mathbf{f}_0^e, \quad \mathbf{s}_0^k = \frac{1}{n_k} \sum_{e=1}^{n_k} \mathbf{s}_0^e \quad \text{and} \quad \mathbf{n}_0^k = \frac{1}{n_k} \sum_{e=1}^{n_k} \mathbf{n}_0^e. \quad (55)$$

To compute the passive stress in (20), we adopt the parameters given in [17]. There, the strain-energy from (23) was fitted to experimental data obtained from an uniaxial extension test and simple shear test conducted simultaneously. For the calculation of the active stress in (20), we use the parameters summarised in Table 6. There, the values were chosen to achieve stable simulations for each method. To account for the electrical flux, the scalar conductivity from

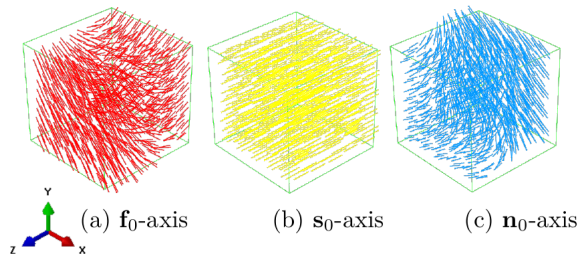


Figure 7: Material  $\mathbf{f}_0$ -,  $\mathbf{s}_0$  and  $\mathbf{n}_0$  - directions for each TET element. The fibre direction  $\mathbf{f}_0$  rotates smoothly from  $+60^\circ$  on the front face to  $-60^\circ$  on the back face with respect to the global  $y$ -axis. The sheet direction  $\mathbf{s}_0$  is aligned to the global  $z$ -axis for each element. The normal direction  $\mathbf{n}_0$  results from the normalised cross-product between  $\mathbf{f}_0$  and  $\mathbf{s}_0$ .

| $\kappa$ [kPa] | $a$ [kPa] | $b$ [-] | $a_f$ [kPa] | $b_f$ [-] | $a_s$ [kPa] | $b_s$ [-] | $a_{fs}$ [kPa] | $b_{fs}$ [-] |
|----------------|-----------|---------|-------------|-----------|-------------|-----------|----------------|--------------|
| 1000           | 1.665     | 1.237   | 7.822       | 0.008     | 0           | 0         | 1.342          | 9.178        |

Table 5: Parameters for passive material response.

| $k_T$ [kPamV $^{-1}$ ] | $a_0$ [mV $^{-1}$ ] | $a_\infty$ [mV $^{-1}$ ] | $\xi$ [mV $^{-1}$ ] | $\varphi_r$ [mV] | $\bar{\varphi}$ [mV] |
|------------------------|---------------------|--------------------------|---------------------|------------------|----------------------|
| 0.0005                 | 1                   | 0.1                      | 0.1                 | -80              | -80                  |

Table 6: Parameters for active material response.

(17) is set to  $d = 0.01 \text{ mm}^2\text{ms}^{-1}$ . We assume that the fibre orientation and resulting orthotropic material behaviour does not affect the spatial propagation of the electric potential. The coupled contraction simulation consists of three steps. In the initial step, the complete cube is polarised at  $-80 \text{ mV}$  for  $1 \text{ ms}$ . In the next step, the nodal potentials in a specific region, depicted in Figure 8 are increased to  $-60 \text{ mV}$  for  $1 \text{ ms}$ . The activated node-set was defined to enable a stable simulation for each method. This activation step triggers the generation of an electric potential and an electric field. As shown in Table 2, the electric potential is generated on the TET mesh for each method. The electric field is either generated on the TET mesh or the SD mesh. In the last step, all electric boundary conditions are omitted. The source term  $I^\varphi$  and governs the generation and temporal evolution of the electric potential and the electric field governs the spatial propagation of the electric potential which results in the deformation of the cube. This contraction step is defined for  $180 \text{ ms}$ . For all steps, the nodes at the cube's top are fixed in each direction to prevent translation. The mechanical boundary condition of the myocardial simulation are depicted in Figure 9. Similar to the dielectric problem, a reference simulation on a hexahedral (HEX) mesh with 125 elements has been conducted to evaluate the accuracy of the numerical methods. In Figure 10, snapshots taken in Abaqus at  $t = 50 \text{ ms}$  for each numerical method are depicted showing the displacement magnitude  $\|\mathbf{u}\|$ . We further evaluate the deformation of the node  $\mathcal{N}$  depicted in Figure 9. The nodal displacement magnitudes over the

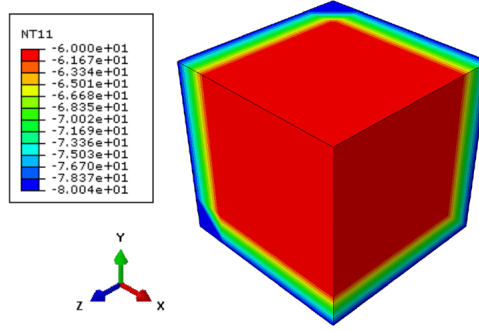


Figure 8: The nodes inside the activation region (red) are depolarised from  $-80$  mV to  $-60$  mV which generates an electric field inside the cube and triggers the generation of electric potential based on the Aliev-Paniflov model.

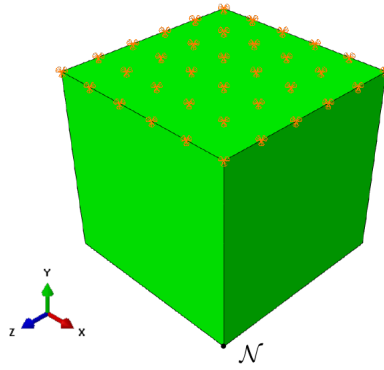


Figure 9: Location of the mechanical boundary conditions for the myocardial cube simulation. The displacement of node  $\mathcal{N}$  are later evaluated.

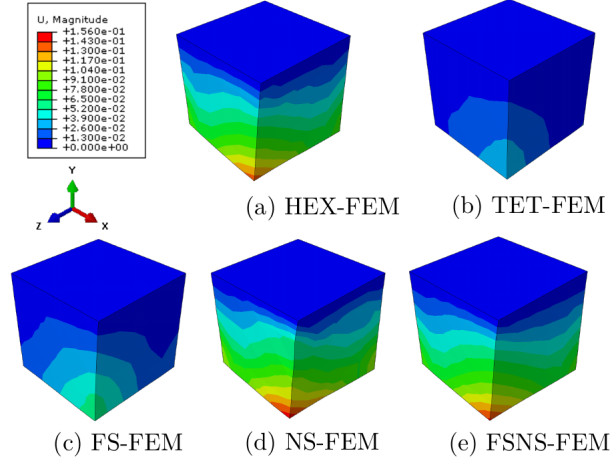


Figure 10: Snapshot taken at  $t = 50$  ms in Abaqus of the displacement magnitude  $||\mathbf{u}||$  in mm for each numerical method.

contraction step time for each numerical method is shown in Figure 11. Similar

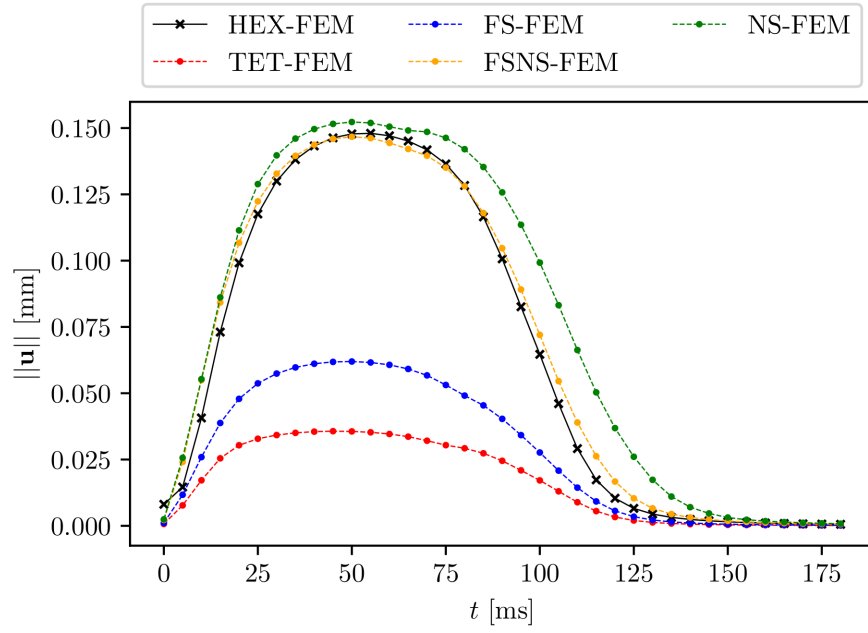


Figure 11: Displacement magnitude of node  $\mathcal{N}$  during the contraction step  $t \in [0, 180]$  ms for each method.

to the DEA cube, the simulation using TET-FEM yields solutions that are a

| method   | $\bar{e}_r$ [-] | CPU time [s] |
|----------|-----------------|--------------|
| TET-FEM  | 0.744           | 15.9         |
| FS-FEM   | 0.57            | 5.1          |
| NS-FEM   | 0.183           | 15.9         |
| FSNS-FEM | 0.056           | 12.4         |

Table 7: Mean relative error  $\bar{e}_r$  over simulation time with respect to the HEX-FEM solution and total CPU time for each numerical method.

lot smaller than the reference solutions. This observation indicates the presence of the volumetric locking phenomena which appears when linear TET elements are used in combination with nearly-incompressible material according to [13]. Using FS-FEM reduces the volumetric locking but the deformation is still below the reference. Using NS-FEM, the deformation is higher than the reference which indicates an overestimated softness, similar to the observation from the DEA example. The results obtained from the FSNS-simulation are the closest to the reference solutions. For each S-FEMs and TET-FEM we again compute  $\bar{e}_r$  using (54). The results are listed in Table 7 together with the total CPU time for each method. The use of TET-FEM results in the largest error with  $\bar{e}_r = 74.4\%$  and takes the longest with a CPU time of 15.9 s. Similar to the DEA example, this method tends to be relatively ineffective. The simulation using FS-FEM runs the fastest but produces the second largest error with  $\bar{e}_r = 57\%$ . The use of NS-FEM also tends to be ineffective regarding an error of  $\bar{e}_r = 18.3\%$  and a CPU time of 15.9 s which is the same time as for TET-FEM. The solution obtained from the FSNS-FEM simulation is the closest to the reference with an error of  $\bar{e}_r = 5.6\%$ . In comparison to FS-FEM, the CPU time of FSNS-FEM is still rather long with 12.4 s. Nevertheless, we still conclude FSNS-FEM to be the most suitable method to simulate the myocardial tissue because it overcomes the volumetric locking with a small enough error which compensates the longer CPU time.

## 6. Conclusion

In this work, we used FEM and various S-FEMs to numerically approximate and solve the electro-mechanically coupled boundary value problem. The commercial software Abaqus was used as a simulation environment. To implement the numerical methods, we created electro-mechanically coupled UELs for TET-FEM, FS-FEM, NS-FEM and FSNS-FEM. We simulated two numerical examples, the electrically induced contraction of a DEA and myocardial tissue. For both examples, we used a cube as benchmark geometry. For DEA example the passive material behaviour was defined with a compressible Neo-Hookean energy function. The active material behaviour was defined based on the ideal dielectric elastomer energy function. The contraction of the cube was induced by applying a temporally changing external potential. To evaluate the accuracy of each method, a reference solution on a HEX mesh was conducted. A

comparison of each method showed, that TET-FEM and FS-FEM overestimate the stiffness of the DEA cube. The results obtained from NS-FEM indicated an overestimation of the softness. The most accurate method was FSNS-FEM which yielded results that were very close to the reference. This accuracy comes with the trade-off of a higher CPU time.

For the the myocardial tissue sample, the results show the appearance of the volumetric locking phenomena for TET-FEM. Using S-FEM reduced the volumetric locking, where the use of FS-FEM still resulted in an overly-stiff behaviour and NS-FEM showed an overestimation of the softness. The simulation using FSNS-FEM produced the most accurate results. Similar to the DEA example, this results also comes with a high CPU time.

In summary, the use of FSNS-FEM tends to be the most suitable method to simulate the behaviour of a dielectric elastomer and myocardial tissue. This approach produces accurate results but with a long CPU time. In comparison to TET-FEM, FS-FEM and NS-FEM, this is still an acceptable trade-off. We note, that the conducted simulation only serve as benchmarks to compare the quality of each numerical method. Especially for the simulation of the myocardium, the analysis needs to be modified to approach a more realistic result. Future work could address the use of a more appropriate geometry and boundary conditions. Regarding the S-FEMs, the source term  $I^\varphi$  also needs to be included into the smoothing operation to achieve a unified smoothed formulation for the temporal and spatial evolution of the electric potential.

**Acknowledgements:** This work is funded by the Deutsche Forschungsgemeinschaft (DFG, German Research Foundation) project no. 496647562.

**Declaration of competing interest:** There is no conflict of interest to declare.

**Supplementary material:** After publication of the final version of the manuscript, an implementation of all the user element subroutines will be available at our Github repository: [https://github.com/TanTran1512/SFEM\\_electromechanics](https://github.com/TanTran1512/SFEM_electromechanics).

## References

- [1] Aliev, R. R. and Panfilov, A. V. (1996). A simple two-variable model of cardiac excitation. *Chaos, Solitons & Fractals*, 7(3):293–301.
- [2] Bonet, J. and Wood, R. D. (1997). *Nonlinear continuum mechanics for finite element analysis*. Cambridge Univ. Press, Cambridge.
- [3] Cai, B. and Zhou, L. (2019). A coupling electromechanical inhomogeneous cell-based smoothed finite element method for dynamic analysis of functionally graded piezoelectric beams. *Advances in Materials Science and Engineering*, 2019(1).



- [4] Eriksson, T. S. E., Prassl, A. J., Plank, G., and Holzapfel, G. A. (2013). Modeling the dispersion in electromechanically coupled myocardium. *International Journal for Numerical Methods in Biomedical Engineering*, 29(11):1267–1284.
- [5] Göktepe, S., Acharya, S. N. S., Wong, J., and Kuhl, E. (2011). Computational modeling of passive myocardium. *International Journal for Numerical Methods in Biomedical Engineering*, 27(1):1–12.
- [6] Göktepe, S. and Kuhl, E. (2009). Computational modeling of cardiac electrophysiology: A novel finite element approach. *International Journal for Numerical Methods in Engineering*, 79(2):156–178.
- [7] Göktepe, S. and Kuhl, E. (2010). Electromechanics of the heart: a unified approach to the strongly coupled excitation–contraction problem. *Computational Mechanics*, 45(2-3):227–243.
- [8] Henann, D. L., Chester, S. A., and Bertoldi, K. (2013). Modeling of dielectric elastomers: Design of actuators and energy harvesting devices. *Journal of the Mechanics and Physics of Solids*, 61(10):2047–2066.
- [9] Holzapfel, G. A., Gasser, T. C., and Ogden, R. W. (2000). A new constitutive framework for arterial wall mechanics and a comparative study of material models. *Journal of Elasticity*, 61(1/3):1–48.
- [10] Holzapfel, G. A. and Ogden, R. W. (2009). Constitutive modelling of passive myocardium: a structurally based framework for material characterization. *Philosophical transactions. Series A, Mathematical, physical, and engineering sciences*, 367(1902):3445–3475.
- [11] Jiang, C., Zhang, Z.-Q., Han, X., and Liu, G.-R. (2014). Selective smoothed finite element methods for extremely large deformation of anisotropic incompressible bio-tissues. *International Journal for Numerical Methods in Engineering*, 99(8):587–610.
- [12] Jiang, C., Zhang, Z.-Q., Liu, G. R., Han, X., and Zeng, W. (2015). An edge-based/node-based selective smoothed finite element method using tetrahedrons for cardiovascular tissues. *Engineering Analysis with Boundary Elements*, 59:62–77.
- [13] Liu, G.-R. (2019). The smoothed finite element method (s-fem): A framework for the design of numerical models for desired solutions. *Frontiers of Structural and Civil Engineering*, 13(2):456–477.
- [14] Liu, G. R., Dai, K. Y., and Nguyen, T. T. (2007). A smoothed finite element method for mechanics problems. *Computational Mechanics*, 39(6):859–877.
- [15] Liu, G. R. and Nguyen, T. T. (2010). *Smoothed finite element methods*. 1st ed. edition.

- [16] Liu, G. R., Nguyen-Thoi, T., Nguyen-Xuan, H., and Lam, K. Y. (2009). A node-based smoothed finite element method (ns-fem) for upper bound solutions to solid mechanics problems. *Computers & Structures*, 87(1-2):14–26.
- [17] Martonova, D., Alkassar, M., Seufert, J., Holz, D., Duong, M. T., Reischl, B., Friedrich, O., and Leyendecker, S. (2021). Passive mechanical properties in healthy and infarcted rat left ventricle characterised via a mixture model. *Journal of the Mechanical Behavior of Biomedical Materials*, 119:104430.
- [18] Martonová, D., Holz, D., Duong, M. T., and Leyendecker, S. (2021). Towards the simulation of active cardiac mechanics using a smoothed finite element method. *Journal of biomechanics*, 115:110153.
- [19] Martonová, D., Holz, D., Duong, M. T., and Leyendecker, S. (2023). Smoothed finite element methods in simulation of active contraction of myocardial tissue samples. *Journal of biomechanics*, 157:111691.
- [20] Martonová, D., Holz, D., Seufert, J., Duong, M. T., Alkassar, M., and Leyendecker, S. (2022). Comparison of stress and stress-strain approaches for the active contraction in a rat cardiac cycle model. *Journal of biomechanics*, 134:110980.
- [21] Mendizabal, A., Bessard Duparc, R., Bui, H. P., Paulus, C. J., Peterlik, I., and Cotin, S. (2017). Face-based smoothed finite element method for real-time simulation of soft tissue. *Medical Imaging 2017: Image-Guided Procedures, Robotic Interventions, and Modeling*.
- [22] Minh Tuan Duong (2014). *Hyperelastic Modeling and Soft-Tissue Growth Integrated with the Smoothed Finite Element Method-SFEM*. Dissertation, Rheinisch-Westfälische Technische Hochschule Aachen, Aachen.
- [23] Nash, M. P. and Panfilov, A. V. (2004). Electromechanical model of excitable tissue to study reentrant cardiac arrhythmias. *Progress in biophysics and molecular biology*, 85(2-3):501–522.
- [24] Nguyen-Thoi, T., Liu, G. R., Lam, K. Y., and Zhang, G. Y. (2009). A face-based smoothed finite element method (fs-fem) for 3d linear and geometrically non-linear solid mechanics problems using 4-node tetrahedral elements. *International Journal for Numerical Methods in Engineering*, 78(3):324–353.
- [25] Nguyen-Thoi, T., Vu-Do, H. C., Rabczuk, T., and Nguyen-Xuan, H. (2010). A node-based smoothed finite element method (ns-fem) for upper bound solution to visco-elastoplastic analyses of solids using triangular and tetrahedral meshes. *Computer Methods in Applied Mechanics and Engineering*, 199(45-48):3005–3027.
- [26] Townsend, N., Kazakiewicz, D., Lucy Wright, F., Timmis, A., Huculeci, R., Torbica, A., Gale, C. P., Achenbach, S., Weidinger, F., and Vardas, P. (2022). Epidemiology of cardiovascular disease in europe. *Nature reviews. Cardiology*, 19(2):133–143.

- [27] Wang, G., Cui, X. Y., Feng, H., and Li, G. Y. (2015). A stable node-based smoothed finite element method for acoustic problems. *Computer Methods in Applied Mechanics and Engineering*, 297:348–370.
- [28] Wang, S., Decker, M., Henann, D. L., and Chester, S. A. (2016). Modeling of dielectric viscoelastomers with application to electromechanical instabilities. *Journal of the Mechanics and Physics of Solids*, 95:213–229.
- [29] World Health Organization (2021). Cardiovascular diseases (cvds).
- [30] Wriggers, P. (2008). *Nonlinear Finite Element Methods*. Springer Berlin Heidelberg, Berlin, Heidelberg.
- [31] Zhao, X., Hong, W., and Suo, Z. (2007). Electromechanical hysteresis and coexistent states in dielectric elastomers. *Physical Review B*, 76(13).
- [32] Zheng, J., Duan, Z., and Zhou, L. (2019). A coupling electromechanical cell-based smoothed finite element method based on micromechanics for dynamic characteristics of piezoelectric composite materials. *Advances in Materials Science and Engineering*, 2019:1–16.